Vertical distribution of ice optical and microphysical properties in Arctic low-level mixed-phase clouds during ACLOUD

Emma Järvinen[1], Franziska Nehlert[1], Guanglang Xu[1], Fritz Waitz[1], Guillaume Mioche[2], Regis Dupuy[2], Olivier Jourdan[2], and Martin Schnaiter[1,3]

[1]Karlsruhe Institute of Technology, Karlsruhe, Germany
[2]Laboratoire de Météorologie Physique (LaMP), Université Clermont Auvergne/OPGC/CNRS, Clermont Ferrand, France
[3]schnaiTEC GmbH, Bruchsal, Germany

Correspondence: Emma Järvinen (emma.jaervinen@kit.edu)

Abstract. Low-level (cloud tops below 2 km) mixed-phase clouds are important in amplifying warming in the Arctic region through positive feedback in cloud fraction, water content and phase. In order to understand the cloud feedbacks in the Arctic region, good knowledge of the vertical distribution of the cloud water content, particle size and phase is required. Here we present seven in-situ vertical profiles of cloud microphysical and optical properties measured in the European Arctic during the

5 ACLOUD campaign. Late spring- and summer-time stratiform clouds were sampled over pack ice, marginal sea ice zone and open ocean surface with cloud top temperatures varying between -15 and -1.5 °C. The results show that, although liquid phase dominates the upper parts of the clouds, ice phase was frequently observed in the lower parts down to cloud top temperatures as warm as -3.8 °C. In the studied vertical cloud profiles the average liquid phase microphysical properties, droplet number concentration, effective radius and liquid water content, varied between 22 and 120 cm^{-3}, 16 and 27 µm, 0.09 and 0.48

10 gm^{-3}, respectively. The average ice phase microphysical properties, ice number concentration, effective radius and ice water content, varied between 0.01 and 35 L^{-1}, 24 and 75 µm, 0.003 and 0.08 gm^{-3}, respectively. The elevated ice crystal number concentrations and ice water paths observed for clouds with cloud top temperatures between -3.8 and -8.7°C can be likely attributed to secondary ice production through rime-splintering. Low asymmetry parameters between 0.69 and 0.76 were measured for the mixed-phase ice crystals with a mean asymmetry parameter of 0.72. The effect of the ice phase for radiative

15 transfer was investigated for the four cloud cases potentially affected by secondary ice production. Generally the ice phase has only a minor effect to the cloud transmissivity and albedo, except in a case where ice phase dominated the upper cloud layer extinction. In this case cloud albedo was increased by 10%. The presented results highlight the importance of accurate vertical information of cloud phase for radiative transfer and provide a suitable data set for testing microphysical parameterisations in models.

1 Introduction

20 Observations have shown that the Arctic region is particularly sensitive to climate change compared to low latitudes (Rigor et al., 2000; Serreze et al., 2009; Previdi et al., 2021). This sensitivity has been hypothesized to be attributed to myriad of feedback mechanisms taking place in the region. One important feedback is related to changes in cloud fraction, water content

and phase. Clouds reflect solar radiation and absorb and re-emit thermal longwave radrion. In the Arctic region low-level

25   mixed-phase clouds are abundant (Curry and Ebert, 1992; Morrison et al., 2012; Mioche et al., 2015). Together with stratiform liquid clouds Arctic mixed-phase clouds have been found be the most important contributors to the Arctic surface radiation balance by inserting a warming cloud radiative effect in most months except a few months in the summer time when the short-wave cloud radiative effect overcomes the longwave effect (Shupe and Intrieri, 2004).

In order to correctly simulate cloud-radiation feedbacks in the Arctic a good understanding of the vertical distribution of

30   the cloud water content, particle size and phase are required (Curry et al., 1996). In-situ observations of cloud vertical profiles provide a basis for improving this knowledge. Vertical profiles of ice particle microphysical properties in low-level startiform clouds over Arctic sea have been reported in the Europen Arctic (Jackson et al., 2012; Lloyd et al., 2015; Mioche et al., 2017) and in coastal Alaska (McFarquhar et al., 2007). Mioche et al. (2017) presented a statistical analysis of cloud vertical profiles combined from four airborne campaigns. The profiles revealed that supercooled liquid dominates the cloud top with

35   ice being more present in the lower parts of the cloud without any significant vertical trend. The average concentration of ice crystals with diameters (D) larger than 100 μm were found to be 3 L^{-1} for stratiform clouds with cloud top temperatures between -3 and -25°C. Similar ice phase vertical structure without clear trend in the microphysical properties were found in the studies of McFarquhar et al. (2007) and Jackson et al. (2012). McFarquhar et al. (2007) reported average concentrations of ice crystals with maximum dimensions greater than 53 μm of 2.8±6.9 L^{-1} for stratiform clouds in autumn with cloud

40   top temperatures varying between -12 and -16°C and Jackson et al. (2012) reported average concentration of ice crystal with maximum dimension greater than 50 μm of 0.27 L^{-1} for similar cloud top temperatures in April. Lloyd et al. (2015) reported four vertical profiles in spring and summer-time stratocumulus clouds and found that higher median ice crystal concentrations, about 3 L^{-1}, were found in summer than in spring, when the mean ice crystal concentrations were around 0.5 L^{-1}.

Ice crystal concentration above 1 L^{-1} in low-level clouds with cloud top temperatures around -5°C likely cannot be explained

45   by primary nucleation due to low number of active ice nucleating particles (INPs) in that temperature range (Kanji et al., 2017) but could be the result of secondary ice production (SIP). For instance, Lloyd et al. (2015) suggested that the summer-time ice crystal concentrations are the result of rime-splintering and, later, Sotiropoulou et al. (2020) showed in a modelling study that the observed ice crystal number concentrations can be explained by rime-splintering and collisional break-up. Also Fridlind et al. (2007) concluded that the ice crystal concentrations observed by McFarquhar et al. (2007) could not be explained by

50   primary nucleation. Additional evidence from rime-splintering was given by Rangno and Hobbs (2001), who reported ice crystal concentrations up to 40 L^{-1} in clouds with cloud top temperatures above -10°C in late spring and summer-time Arctic stratiform clouds. The most recent evidence of SIP in Arctic low-level clouds was provided by Pasquier et al. (2022), where the authors found that SIP occurred during 40% of the in-cloud measurements in the temperature range from -1 to -24°C performed with a tethered balloon system during the Ny-Ålesund AeroSol Cloud ExperimENT (NASCENT).

55   Albeit the increasing amount of in-situ observations in the Arctic region, not enough is known of the concentration and vertical profiles of small ice crystals. Yet, the vertical distribution of small (<50 μm) ice particles is important to understand both radiative transfer as well as ice initiation through heterogeneous ice nucleation or through SIP, which are key processes controlling the longevity of the Arctic mixed-phase clouds (Morrison et al., 2012). Furthermore, previous vertical profiles of

low-level Arctic clouds have predominantly performed over open ocean (Jackson et al., 2012; Lloyd et al., 2015; Mioche et al., 2017) or over coastal areas (McFarquhar et al., 2007), whereas vertical cloud in-situ profiles over Arctic pack ice have not been studied extensively. Therefore, this work aims to increase the observational knowledge on the vertical phase composition of Arctic mixed-phase clouds mainly over pack ice by presenting in-situ cloud microphysical observations from the Arctic CLoud Observations Using airborne measurements during polar Day (ACLOUD) campaign that was carried out north-west of Svalbard (Norway) between 23 May and 6 June 2017. During ACLOUD a suit of newer cloud probes were deployed for detection of small ice particles down to $D = 9$ μm. Here we present vertical profiles of liquid and ice phase microphysical and optical properties in seven cloud cases, where cloud top temperatures ranged from -15 to -3°C. The vertical information on both liquid and ice phase microphysical properties makes the data set particularly well suited for testing cloud microphysical parameterisations in models. We also present the the vertical variability of the ice particle asymmetry parameter in Arctic low-level mixed-phase clouds retrieved on single-particle nephelometer measurements and discuss the implications of ice phase for the radiative properties of the low level clouds.

2 Details of the field experiment

2.1 Meteorological situation

The ACLOUD aircraft campaign performed 22 research flights between 23 May and 26 June 2017 from Svalbard towards the Arctic ocean. The synoptic development during ACLOUD can be separated into three periods (Knudsen et al., 2018). During the first days of the campaign a seasonally unusual cold air outbreak brought cold and dry Arctic air from the north. This cold period (23 to 29 May) was followed by a warm period (30 May to 12 June) with warm and moist air intrusion into the region caused by a strong southwesterly flow due to a high pressure system located over the Greenland Sea. During 11 and 12 June, northerly winds started to dominate the lower troposphere, indicating the end of the moist air intrusion and the beginning of a normal period (13 to 26 June) where both the temperature and moisture were close to long-term averages recorded in Ny-Ålesund.

2.2 Flight procedure

The objectives of the ACLOUD campaign included the characterisation of Arctic boundary-layer clouds and their vertical profiles over different surfaces (open ocean, marginal sea ice zone and pack ice). In this context, research flights were performed in a sector northwest from Longyearbyen, which was the base of the operations. Vertical profiles were measured in-situ either by flying a double-triangle pattern, where altitude was changed at the outer vertices, or by flying stacked horizontal legs. In-cloud sampling during one horizontal leg usually lasted between 7 to 10 minutes, which allows enough statistics for deriving cloud microphysical properties from single-particle spectrometers.

2.3 Instrumentation

The Polar 6 was equipped with in-situ instrumentation for the characterisation of cloud hydrometeors, aerosol particles and
90   trace gases. The cloud instrumentation included the following three instruments used here:

- The Small Ice Detector Mark 3 (SID-3; Hirst et al. (2001)), which detects individual cloud particles passing a 532 nm laser beam using two nested trigger detectors with a half angle of $9.25°$ symmetrically located at $50°$ relative to the forward direction. The trigger signal is recorded as a histogram that can be used to derive particle size distributions by using the procedure described in Vochezer et al. (2016). Particle size distributions are issued in the ACLOUD data set (Schnaiter and Järvinen, 2019a). The maximum acquisition rate of the trigger detector is 11 kHz. For a sub-set of triggered particles a two-dimensional (2-D) scattering pattern is recorded that can be analysed for particle sphericity (Vochezer et al., 2016) and crystal complexity in case of ice crystals (Schnaiter et al., 2016) by a specifically developed image analysis software. Particle shape and ice crystal complexity distributions are issued in the ACLOUD data set (Schnaiter and Järvinen, 2019b). An analysis of the ice crystal complexity that has been observed during ACLOUD is published in Järvinen et al. (2018). Occasionally, coincidence sampling in the camera field of view causes optical distortions of the 2-D scattering patterns and, consequently, a misclassification of such scattering patterns to be aspherical by the classification software. For the subsequent identification and re-classification of coincidence scattering patterns a machine learning (ML) algorithm was developed (see Appendix A for details).

- The Particle Habit Imaging and Polar Scattering (PHIPS) probe, which is a combination of a polar nephelometer and a high-resolution cloud particle stereo-imager (Abdelmonem et al., 2016; Schnaiter et al., 2018; Waitz et al., 2021). The two parts of the instrument are combined by a trigger detector so that both imaging and scattering measurements are performed on the same single particle. The polar nephelometer has 20 channels ranging from 18 to $170°$, with an angular resolution of $8°$. The measured single-particle light scattering functions (Schnaiter and Järvinen, 2019c) can be used to derive particle sphericity and size distributions of spherical and aspherical particles using the methods discussed in Waitz et al. (2021). Here particle size distributions were calculated for 10-s time resolution corresponding to a lower detection limit of about 2 L^{-1}. The uncertainties in the number concentrations of droplets and ice particles are 20% and 40%, respectively (Järvinen et al., 2022). The stereo-microscopic imager consists of two camera and microscope assemblies with an angular viewing distance of $120°$ acquiring bright field stereo-microscopic images of individual cloud particles. During ACLOUD, two different magnifications of 6x and 8x were set for the two PHIPS microscopes of camera 1 and 2 corresponding to optical resolutions of $\sim$3.5 μm and $\sim$2.3 μm, respectively.

- The Cloud Imaging Probe (CIP; Baumgardner et al. (2001)), which uses a linear-array technique to acquire two-dimensional shadow images of cloud particles. The CIP has a nominal size range from 25 to 1550 μm with 25 μm pixel-resolution. Ice phase cloud particles are separated from liquid phase particles following the approach of Crosier et al. (2011) based on a circularity parameter (circularity larger than 1.25 and image area larger than 16 pixels). Only these non-spherical particles were used to calculate ice-phase properties. The ice particle size distributions were cal-

culated for non-spherical particles using area-equivalent diameter. Possible contamination by shattering artifacts were removed using inter-arrival time analysis and image processing according to Field et al. (2006). The remaining combined uncertainty in the number concentration is 50% (Baumgardner et al., 2017). The resolution of the CIP data products is given in 1-Hz (Dupuy et al., 2019) and here we averaged the data over 10-s periods to increase the counting statistics

125   corresponding a lower detection limit of 0.01 L^{-1}.

On Polar P6 high-frequency measurements of wind vector and air temperature were performed in a nose boom using an Aventech five-hole probe and an open-wire Pt100 installed sidewards in a Rosemount housing (Hartmann et al., 2018). Humidity was measured with 1-Hz resolution with a Vaisala HMT-333, which includes a temperature and HUMICAP humidity sensor. Based on the temperature measurements (uncertainty of 0.1 K), the humidity data were corrected for adiabatic heating

130   (Hartmann et al., 2018). In this paper we use merged thermodynamic measurements providing aircraft position, air pressure, temperature, relative humidity, and the horizontal wind vector at a resolution of 1-Hz (Hartmann and Chechin, 2019). Aerosol particle concentration in the nominal size range from 60 to 1000 nm were measured with the ultra-high sensitivity aerosol spectrometer (UHSAS, Cai et al. (2008)) that was installed behind the counter-flow virtual impactor (CVI) (Mertes, 2019).

2.4   Calculation of microphysical and optical parameters

135 ### 2.4.1   Concentrations of spherical and aspherical particles

Total concentration of spherical particles in the size range from 5 to 700 μm was calculated by combining the total concentration of spherical particles measured by SID-3 (between 5 and 42 μm) and PHIPS (between 60 and 700 μm). No extrapolation was performed to cover the missing size range between 42 and 60 μm as the concentration and LWCs of spherical particles measured by PHIPS were typically more than two magnitudes lower than spherical particles measured by SID-3.

140   Total concentration of aspherical particles in the size range from 9 to 1550 μm was calculated by combining the total concentration of aspherical particles measured by SID-3 in the size range from 9 to 30 μm, the total concentration of aspherical particles measured by PHIPS in the size range from 30 to 200 μm and the total concentration of aspherical particles measured by the CIP in the size range from 200 to 1550 μm. The size limits were chosen to maximise the counting statistics and optimise phase discrimination certainty. Occasionally, indications of shattering were seen in the PHIPS data and sometimes also in

145   the SID-3 data (see supplementary information). If shattering was observed, the PHIPS and SID-3 data were removed from analysis so that the total concentrations were only given for particles >200 μm measured by CIP.

2.4.2   LWC, IWC, LWP and IWP

The LWC (IWC) for each cloud microphysical probe was calculated using the following equation

$$LWC(IWC) = \sum_{D_{min}}^{D_{max}} n(D)M(D),$$ (1)

150   where $n(D)$ is the number of spherical (aspherical) particles in a size bin and $M(D)$ is the mass of a particle having a diameter corresponding to the bin mean diameter. For derivation of LWC, $M(D)$ was calculated for spherical particles with a density of

$1\,\mathrm{g\,cm^{-3}}$. For derivation of IWC from SID-3 measurements $M(D)$ was calculated assuming spherical particles with a density of $0.91\,\mathrm{g\,cm^{-3}}$. IWC was calculated from PHIPS and CIP measurements $M(D)$ using the mass-dimensional relationship from Brown and Francis (1995)

$$M(D) = aD^b, \tag{2}$$

where $a = 7.38 \times 10^{-11}$ and $b = 1.9$.

The total LWC is the sum of LWCs derived from the SID-3 (size range from 5 to 42 µm) and PHIPS (size range from 60 to 700 µm). The total IWC is the sum of the IWCs derived from the SID-3 (size range from 9 to 30 µm), PHIPS (size range from 30 to 200 µm) and CIP (size range from 200 to 1550 µm).

The integrated liquid and ice water paths were calculated from in-situ measurements according to the following equation

$$WP = \int_{ground}^{cloud\,top} WCz\,dz, \tag{3}$$

where WP is either the liquid water path (LWP) or ice water path (IWP), WC either LWC or IWC and z is the height between ground and cloud top.

2.4.3 Extinction coefficient and effective diameter

The extinction coefficient was calculated using the following equation

$$\beta_{ext} = \sum_{D_{min}}^{D_{max}} n(D)\sigma(D), \tag{4}$$

where $\sigma(D)$ is the scattering cross section of a particle having a diameter corresponding to the bin mean diameter.

For spherical particles in the SID-3 size range, the $\sigma(D)$ was calculated using the Mie theory. For PHIPS and CIP size range geometrical optics assumption was used, where the scattering cross section is two times the geometrical cross section.

For calculating the effective radius (r_{eff}) we used the following definition

$$r_{eff} = \frac{3WC}{2\rho\beta_{ext}}, \tag{5}$$

where ρ is the bulk density of water or ice.

2.4.4 Ice crystal asymmetry parameter

The asymmetry parameter (g) of ice crystal ensembles was retrieved from the average ice crystal angular scattering functions following the method presented in Xu et al. (2022). The retrieval is based on the assumption that in geometrical optics range, the following relation can be used to derive asymmetry parameter,

$$g = \frac{1}{2\omega_0}[(2\omega_0 - 1)g_{GO} + g_D], \tag{6}$$

where g_{GO} and g_D are the asymmetry parameter contributed by geometric-optics and diffraction, respectively. As the diffraction phase function is highly peaked, g_D is very close to unity. According to the analysis of scalar diffraction theory, most

180   of the diffracted energy will be confined into the angular range of $\theta < 7/x$ (in radian), where x is the size parameter. On a logarithmic scale, $g_D(d)$ can be approximated by a polynomial of degree 4, i.e,

$$g_D(d) = -5.9270 \times 10^{-5} - 0.00130 \times ln(d) - 0.01087 \times (ln(d))^2$$
$$+ 0.04093 \times (ln(d))^3 + 0.94029 \times (ln(d))^4, \tag{7}$$

where d is the particle diameter. The geometric-optics contribution g_{GO} can be obtained from polar nephelometer measurements by extrapolating the measurements by applying Gaussian quadrature. One g value was calculated for each altitude within

185   the cloud if a minimum of 20 ice particles were observed by PHIPS to assume an orientation averaged population.

2.5 Habit classification

Ice crystal habits were manually classified using a classification scheme following Bailey and Hallett (2009). They proposed a habit diagram with the main distinction between single crystals and polycrystals and columnar and plate-like subsections. Each subsection includes several habits. In our manual habit classification we apply a tree-based classification scheme. On the

190   main node we distinguish between single and polycrystals. The next level is the subdivision into plate-like, column-like and mixed growth. The leaf nodes are the habits, namely plate, sectored plate, skeletal plate, dendrite, column, needle, bullet, side plane, bullet rosette, needle rosette, capped column, capped bullet rosette and mixed rosette. Depending on the image quality, crystal size and orientation, classification is done to the level where it can clearly be determined. When a polycrystal cannot be assigned to a specific habit, but the growth direction is detectable, it falls into one of the following categories: other poly plate,

195   other poly column or other column-plate mix. When the growth direction of a polycrystal is not detectable, it will be classified as other polycrystal. In addition to its habit, attributes like riming and aggregation, were assigned to each ice crystal.

3 Vertical profiles of cloud microphysical properties

During ACLOUD low-level clouds (cloud tops below 2 km) were observed in the study area (Fig. 1) on all measurement days. Space-borne remote sensing observations showed that the cloud top heights decreased during the warm period compared to

200   the cold period, whereas during the normal period higher and more variable cloud tops were observed (see Fig. 3 in Wendisch et al. (2019)). Here we discuss the detailed vertical profiles of cloud microphysical and optical properties measured during the three meteorological regimes. For warm and normal period the vertical profiles are given as a function of normalised cloud altitude, Z_n, which is defined as following (Mioche et al., 2017)

$$Z_n = \frac{Z - Z_b}{Z_t - Z_b} \quad \text{for } Z_b < Z < Z_t$$

205

$$Z_n = \frac{Z}{Z_b} - 1 \quad \text{for } Z < Z_b$$
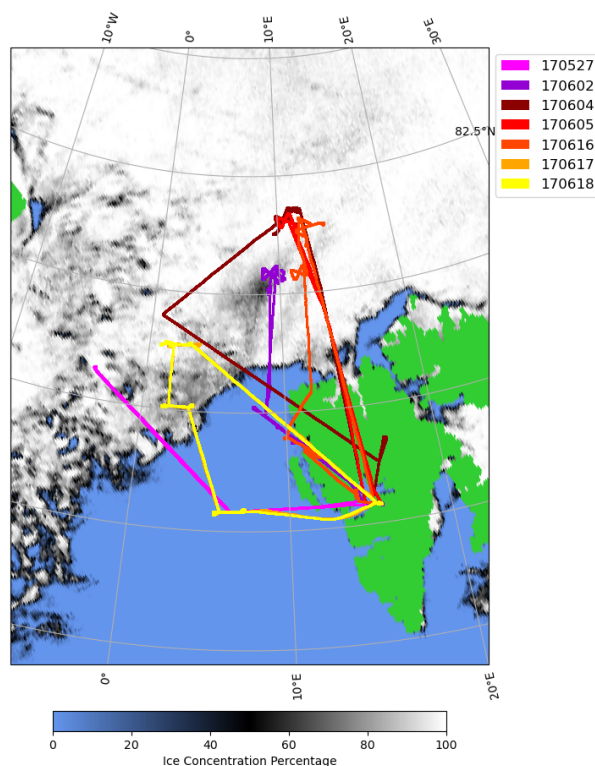
Figure 1. Flight paths for the ACLOUD flights with Polar 6 aircraft included in the analysis overlaid on pack ice extend as of 2 June. pack ice data is derived from measurements of the Advanced Microwave Scanning Radiometer 2 (AMSR2) at 89 GHz (www.seaice.uni-bremen.de; Spreen et al. (2008)).

where Z is the altitude corresponding aircraft measurements, and Z_t and Z_b the cloud liquid layer top and base, respectively. A threshold LWC of $0.01 \ \mathrm{g \, m^{-3}}$ was used to define the liquid layer top and base. A detailed list of the vertical cloud profiles can be found in Table 1.

3.1 Vertical profile over marginal sea ice zone during cold period on 27 May

On 27 May a research flight was performed off the west coat of Svalbard, where stratus clouds were sampled over the marginal sea ice zone between 79.8 and 78.6°N. Figure 2 shows the vertical profile of temperature during the period of cloud sampling. No clear temperature inversion was observed on this day. The sampled cloud system was multi-layered consisting of cloud layer between 1080 and 1317 m with a cloud top temperature of -15.2°C and a lower cloud layer ranging between 186 and 630 m with a cloud top temperature of -11°C. Precipitation was observed between the cloud layers.

The multi-layered cloud system was sampled in one ascent with three straight legs performed in the lower cloud at altitudes of 490, 410 and 360 m. The mean vertical profiles of liquid cloud properties are shown in Figure 3. Mean cloud droplet number concentration up to $22 \ \mathrm{cm^{-3}}$ were observed in the upper cloud layer and somewhat higher mean droplet concentrations up
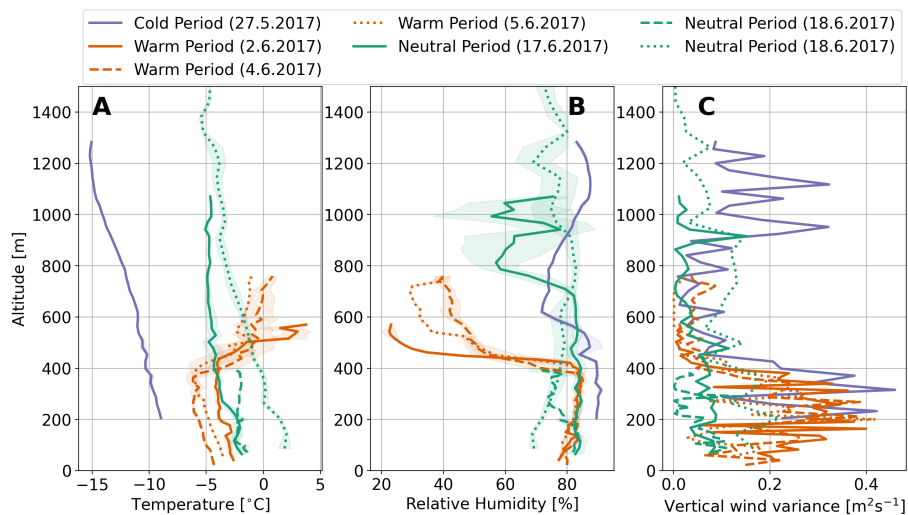
Figure 2. Average temperature (A), relative humidity (B) and vertical wind variance (C) for the vertical profiles performed during cold period (blue), warm period (red) and neutral period (green). Note that the solid lines describe the average values during the entire sampling period. The shaded area in A and B shows the standard deviation.

Table 1. Vertical cloud profiles included in the study. For each profile the cloud top temperature (T), liquid water path (LWP), ice water path (IWP) and aerosol number concentration (N_a) for aerosol particles with D >60 nm is given.

Date	Cloud Top T	LWP	IWP	N_a above
	°C	$g\,m^{-2}$	$g\,m^{-2}$	cm^{-3}
Cold Period				
27 May	-15.2	41.4	1.0	73
Warm Period				
2 June	-4.5	85.4	10.0	175
4 June	-6.7	60.0	4.1	126
5 June	-6.4	49.5	7.4	134
Normal Period				
17 June	-5.2	37.4	9.5	162*
18 June	-3.0	13.0	0.004	-
18 June	-5.2	27.4	44.3	-

*below cloud value
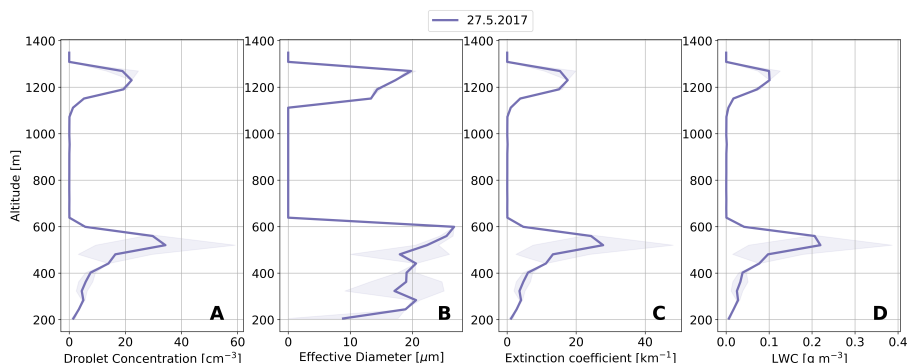
Figure 3. Vertical profile of droplet concentration (A), droplet effective diameter (B), droplet extinction coefficient (C) and liquid water content (LWC) (D) performed on 27 May during the cold period. The shaded area illustrates the standard deviations.
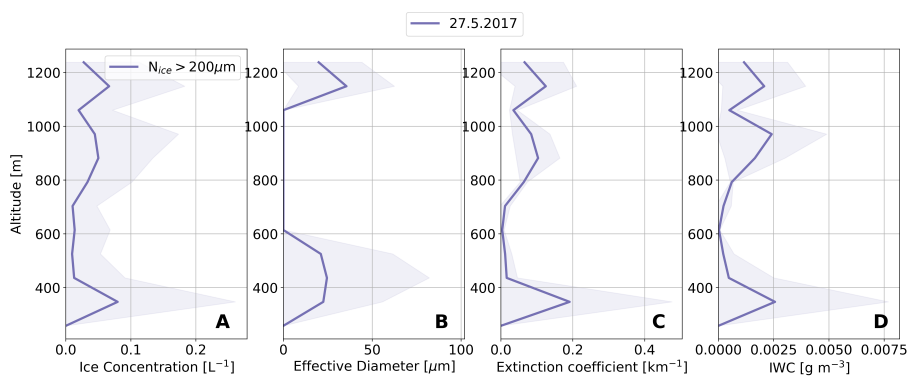
Figure 4. Vertical profile of concentration of ice particles with D >200 µm (A), ice particle effective diameter (B), ice particle extinction coefficient (C) and ice water content (IWC) (D) performed on 27 May during the cold period. The shaded area illustrates the standard deviations. Note that ice particle microphysical properties were retrieved using only CIP due to observed shattering in PHIPS and SID-3 probes.

to 35 cm^{-3} were observed in the lower cloud layer. The effective diameter was observed to increase with altitude with larger

220   mean effective diameters up to 27 µm observed in the lower cloud layer compared to the upper cloud layer where the mean effective diameters up to 20 µm were observed. A few large (D>60 µm) drizzle droplets were observed in the PHIPS images in the cloud layers. LWC mean values of 0.1 and 0.2 $\mathrm{g\,m}^{-3}$ and extinction coefficient of 18 and 28 km^{-1} were observed in the upper and lower cloud, respectively. However, it should be noted that the lower cloud layer was sampled closer to the pack ice edge compared to the upper cloud layer, which might explain some of the differences seen in the microphysical properties.

225   The liquid cloud properties observed during the cold period case study were similar to what McFarquhar et al. (2007) observed during the Mixed-Phase Arctic Cloud Experiment (M-PACE) for clouds with similar cloud top temperature but the observed droplet concentrations were lower by a factor from 2 to 4 than observed in other similar cold air outbreak situations in Arctic
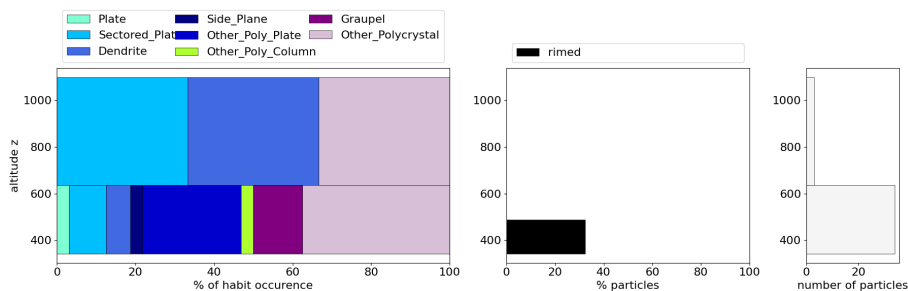
Figure 5. Analysis of ice crystal habits during cloud sampling on 27 May. The bar between 1317 and 630 m represents the habits in the upper cloud and in the precipitation zone. The lower bar represent the habits in the lower cloud.

clouds reported by Lawson et al. (2001), Jackson et al. (2012) and Mioche et al. (2017). However, these differences can be partly explained by the fact that these previous measurements were conducted over open water. For example, Mioche et al.

230 (2017) observed similar LWC in cold air outbreak influenced clouds but these clouds had effective droplet diameters around 15 μm.

Figure 4 shows the vertical profiles of ice phase microphysical properties. Only CIP was used to retrieve ice phase properties for ice particles larger than 200 μm in diameter due to indications of shattering observed in the PHIPS stereo-images. For precaution, also SID-3 ice data was excluded from the analysis. From those PHIPS stereo-images that were not influenced by

235 shattering it can be seen that the dominant habits in the multilayered cloud system were dendrites, sectored plates and other polycrystaline plates (Fig. 5) in accordance with laboratory studies of Bailey and Hallett (2009). Riming was also present in the lower cloud layer. The concentration of ice particles with $D >$200 μm were on average between 0.01 and 0.08 L^{-1}, which is comparable to expected INP concentrations for cloud top temperature of -15°C (Kanji et al., 2017). Therefore, primary ice nucleation could explain the observed ice particle number concentrations. The low ice crystal concentrations translate to low

240 IWC below 0.003 g m^{-3} and extinction coefficient below 0.2 km^{-1}. Ice crystal effective diameter was around 40 μm in the upper cloud and 24 μm in the lower cloud.

3.2 Vertical profiles over pack ice during warm period on 2, 4 and 5 June

On 2 June the moist and warm air intrusion caused development of cloudiness to the Svalbard area and a fairly uniform low-level cloud deck was observed starting from Ny Ålesund reaching to Polarstern pack ice camp. On the following days the

245 uniform cloud deck persisted. On 2, 4 and 5 June three vertical cloud profiles were performed near Polarstern sampling the low-level cloud deck over pack ice (Fig. 1). Figure 2 shows that on those three days similar vertical profiles of temperature were observed with cloud top temperatures between -4.6 and -6.7°C capped by a strong temperature inversion of about 8°C. Inversion is a dominant feature in the Arctic environment, particularly during the coldest half of the year (e.g., Kahl, 1990; Kahl et al., 1992; Serreze et al., 1992). On all three days a single layer cloud was observed with occasional visible cirrus clouds

250 in the horizon. Cloud tops were observed to be around 400 m and cloud heights varied between 280 and 340 m.
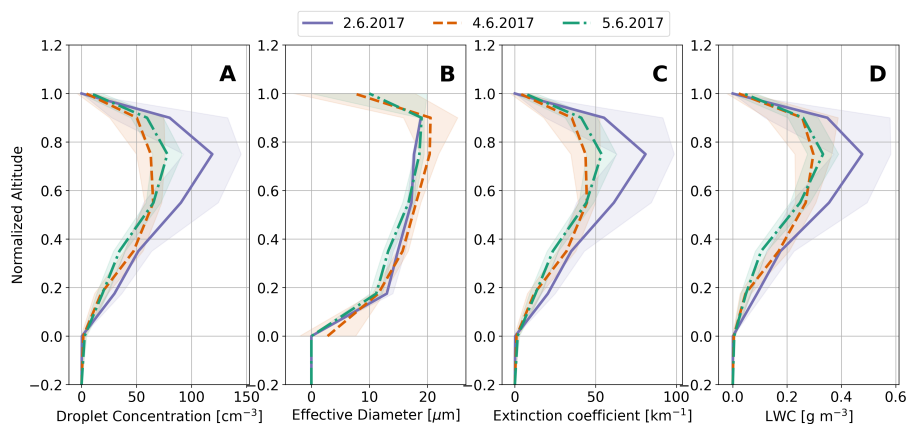
Figure 6. Vertical profile of droplet concentration (A), droplet effective diameter (B), droplet extinction coefficient (C) and liquid water content (LWC) (D) performed on 2, 4 and 5 June during the warm period. The shaded area illustrates the standard deviations.

The observed mean vertical profiles of liquid cloud properties were similar for the three days where the stratiform cloud was sampled near Polarstern over pack ice (Fig. 6). All profiles are characterised by increasing values of droplet concentration, effective droplet diameter, extinction coefficient and LWC with increasing altitude until $Z =$ 0.75 and a subsequent decrease. Droplet concentrations around $Z_n =$ 0.75 were the highest on 2 June, on average 120 $\mathrm{cm^{-3}}$ and decreased to 64 (79) $\mathrm{cm^{-3}}$ on

255   4 June (5 June). This decrease in droplet concentrations correlates with the decrease in aerosol number concentration above the clouds measured by the UHSAS from 173 $\mathrm{cm^{-3}}$ to 126 (134) $\mathrm{cm^{-3}}$. The effective droplet diameters were on all days around 20 µm near cloud top. The extinction coefficient and LWC were highest on 2 June, 82 $\mathrm{km^{-1}}$ and 0.48 $\mathrm{g\,m^{-3}}$, respectively, compared to 4 and 5 June where the values were around 50 $\mathrm{km^{-1}}$ and 0.3 $\mathrm{g\,m^{-3}}$, respectively. The clouds sampled during the warm period contained 2 to 4 times more droplets and larger LWC by a factor of 1.5 to 3 compared to the cold period cloud

260   case, which can be explained by the intrusion of moister air with higher aerosol load. Comparison with theoretical adiabatic LWC profiles (not shown here) showed that the clouds measured during warm period were superadaiabatic, which might be the result of stronger updrafts, entrainement of humid air from above or radiative cooling at cloud top for instance. The observed LWC values over pack ice were similar to what was observed in similar warm air intrusion situations by Mioche et al. (2017) over open sea surface but lower (by a factor of 3) than the LWC in clouds measured over open sea surface during ACLOUD

265   (Dupuy et al., 2018).

Figure 7 shows the mean vertical profiles of ice phase microphysical properties. Concentration of small ice could be only derived for the upper half of the cloud due to observed shattering in the lower parts of the cloud. All profiles are characterised by a slight increase of IWC and extinction coefficient with decreasing altitude. However, definite trends in IWC cannot be made due to uncertainties linked with mass-dimensional relationship used to calculate IWC. Very little ice was observed at the cloud

270   top indicating that the cloud top layer is almost exclusively composed of supercooled liquid droplets. Due to the missing small ice information in the lower parts of the cloud, it cannot be concluded if the ice crystal number concentration would have a
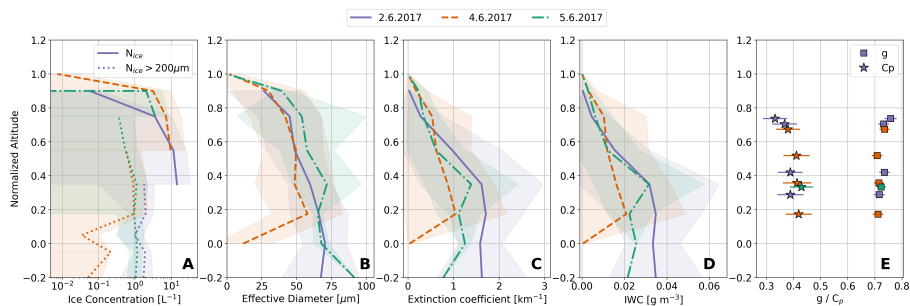
Figure 7. Vertical profile of ice particle concentration (N_{ice}) (A), ice particle effective diameter (B), ice particle extinction coefficient (C) and ice water content (IWC) (D) performed on 2, 4 and 5 June during the warm period. The shaded area illustrates the standard deviations. Note that ice particle microphysical properties in the lower parts of the cloud were retrieved using only CIP for ice crystals D > 200 μm ($N_{ice>200\mu m}$) due to observed shattering in PHIPS and SID-3 probes. Panel E shows the asymmetry parameter (g) and complexity parameter (C_p) derived from PHIPS. One value was derived for each straight leg within the cloud. The horizontal error bars illustrate the retrieval uncertainty.

maximum or if the ice crystal concentrations would be independent of Z_n below Z_n =0.7. The maximum measured ice crystal concentration varied between 4 and 15 L^{-1}. The effective diameters varied between 50 and 75 μm, extinction coefficients between 1 and 2 km^{-1}, and IWC between 0.02 and 0.04 g m^{-3}. The observed ice particle concentrations were two orders of magnitude higher during the warm period than observed in the cold period cloud case, and four orders of magnitude higher than expected INP concentrations at -5°C indicating potential ice production by SIP.

The vertical distribution of particle shape was also investigated using the PHIPS stereo-microscopic images for indications of ice formation and growth processes (Fig. 8). The dominant ice habits were single crystals in the form of needles (31.0 %) and columns (16.4 %). This is in contradiction to previous studies where irregular (polycrystal) habits have been found to dominate Arctic mixed-phase clouds (Korolev et al., 1999; Mioche et al., 2017). A significant fraction (38.5 %) of the observed ice crystals were rimed. During all days an increase in rimed particle fraction was observed with increasing cloud height but no definite conclusions about the vertical structure in riming can be made due to the low statistics. It is likely that the occurrence of rimed needles and graupel together with faceted unrimed small needles and columns indicates rime-splintering processes.

The observed ice crystal concentrations during the warm period were significantly higher than what was observed by Mioche et al. (2017) and McFarquhar et al. (2007) although the effective diameters were similar to the previous studies. SIP in arctic clouds with cloud top temperatures above -8°C have been reported by Rangno and Hobbs (2001) and Pasquier et al. (2022). Rangno and Hobbs (2001) observed ice crystal concentration up to 40 L^{-1} in Arctic stratocumulus clouds in late spring and early summer. Their type III slightly supercooled startiform clouds, containing droplets with D >28 μm and high ice crystal concentrations, explain well our observations during the warm period. Pasquier et al. (2022) explained that high (>50 L^{-1}) ice concentrations at temperatures above -5°C were related to SIP by droplet shattering mechanism. In our case superadiabatic LWC profiles could have indicated larger droplets and in all warm period cases drizzle droplets were observed. Large droplets

(a) 2 June

(b) 4 June
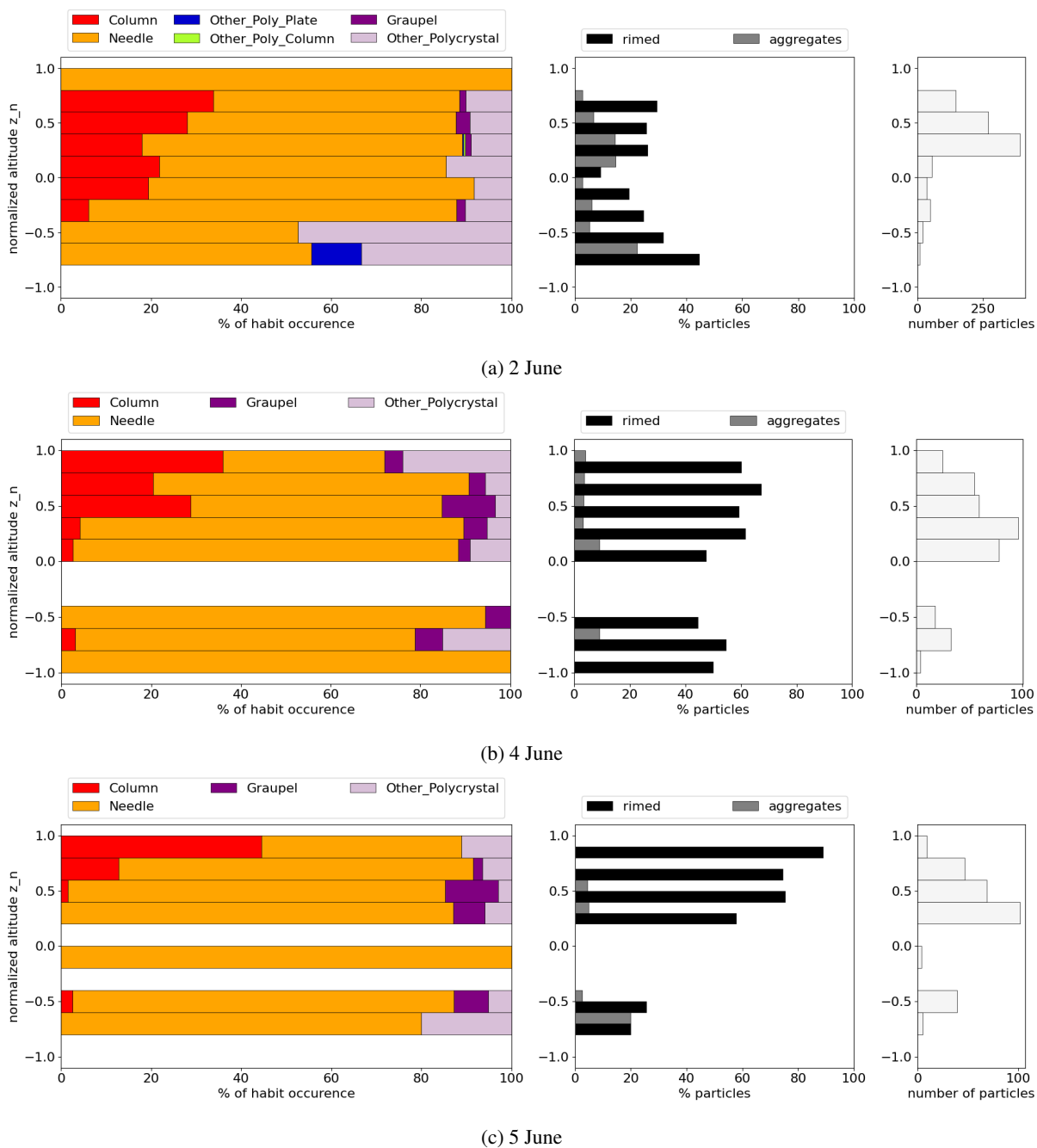
(c) 5 June

Figure 8. Analysis of ice crystal habits during cloud sampling on 2, 4 and 5 June during warm period.

could promote either droplet shattering or enhance rime-splintering rate (Mossop, 1985). During M-PACE campaign SIP was not discussed by McFarquhar et al. (2007) but a later modelling study using the Community Atmosphere Model version 6
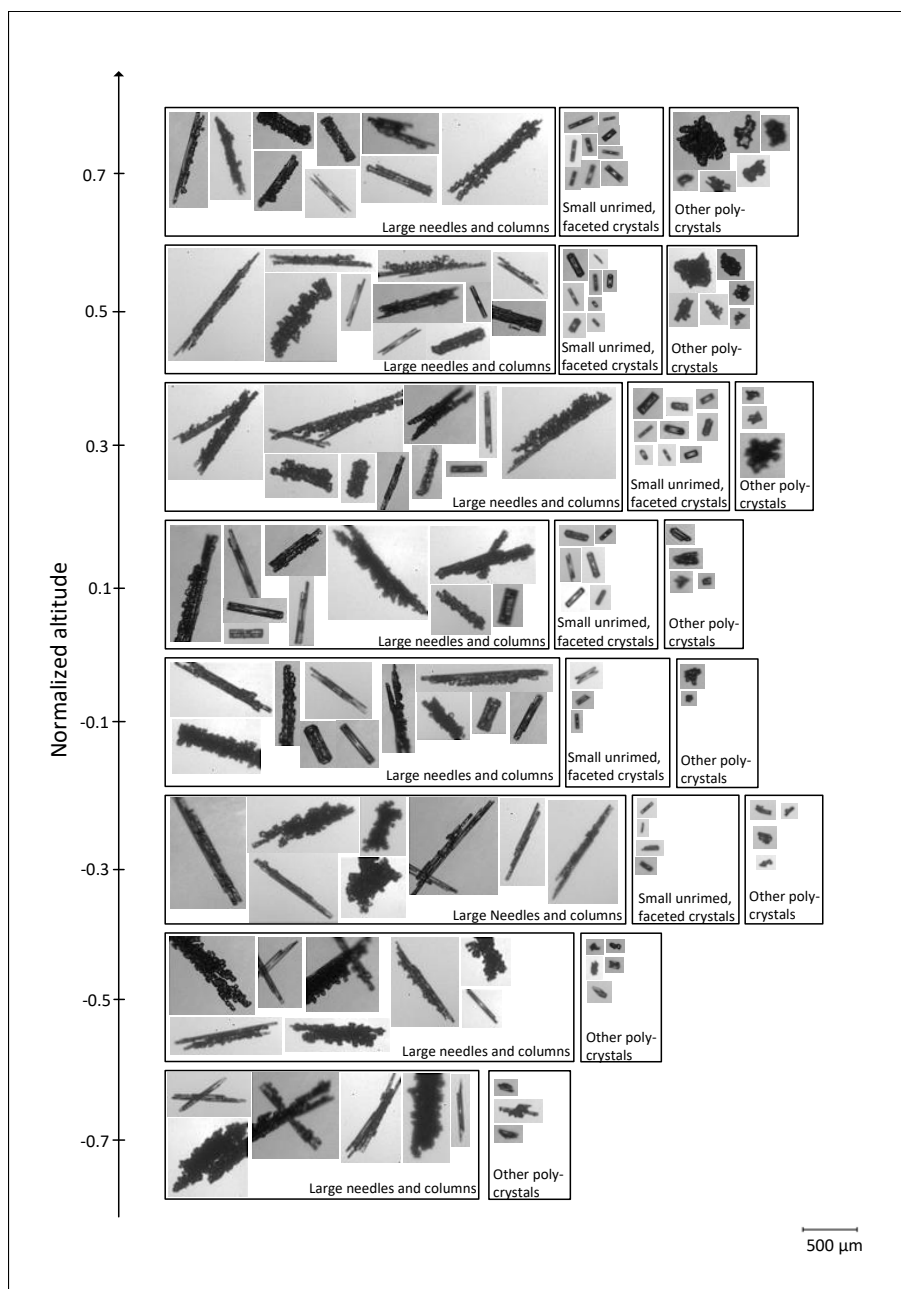
Figure 9. Example ice crystal habits as a function of normalised altitude measured on 2 June during the warm period.

(CAM6) by Zhao et al. (2021) showed that inclusion of SIP in the model was important for improving the model representation

295   of the observed cloud situations.
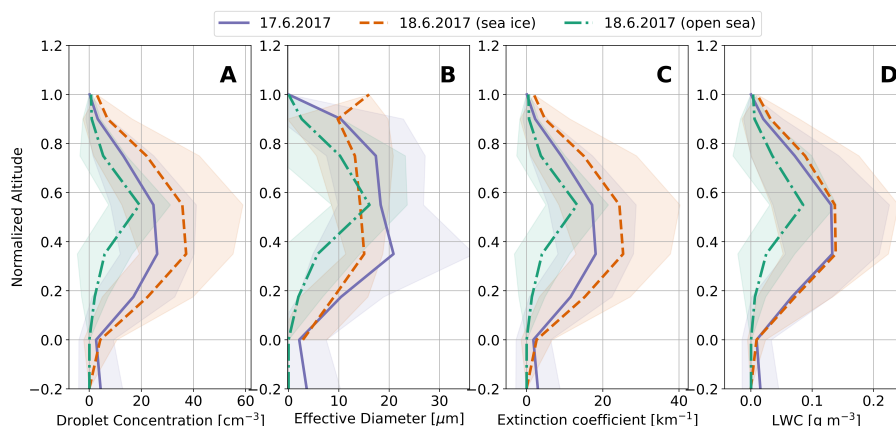
Figure 10. Vertical profile of droplet concentration (A), droplet effective diameter (B), droplet extinction coefficient (C) and liquid water content (LWC) (D) performed on 17 and 18 June during the normal period. The shaded area illustrates the standard deviations.

3.3 Vertical profiles during normal period on 17 and 18 June

In the final two weeks of the ACLOUD campaign, adiabatically warmed air from the west and north dominated the study region (Knudsen et al., 2018) leading to more variable cloud properties (Wendisch et al., 2019). On 16 June northerly flows brought colder air from north and west of Svalbard to the study region generating a solid cloud deck from Svalbard to Polarstern vessel.

300 On the following days the cloud deck persisted but became spatially more inhomogeneous often with multi-layered structure. On 17 and 18 June cloud profiling was performed over pack ice near Polarstern and on 18 June also over open sea surface (Fig. 1. On 17 June the cloud system near Polarstern consisted of a more mixed lower layer topped with a thin stratus layer. The thicker lower layer had cloud top at 704 m at -5.4°C without a temperature inversion (Fig. 2). The cloud base was at 85 m around -2°C and precipitation was observed below the cloud. On 18 June the cloud top over pack ice was lower at 417 m with

305 cloud top temperature of -3.0°C. The cloud base was at 65 m. Over the open water the startocumulus layer differed significantly from the layer measured over pack ice: strong convective clusters penetrating through the startocumulus deck from below were observed. The convective clusters were separated from each other by large distances of order of 10 km. The cloud top was located at 1323 m with a very weak temperature inversion around 1°C. The cloud top temperature was -5.2°C. The cloud base was located at 300 m with precipitation in the form of snow observed below.

310 Figure 10 shows the vertical profiles of the average cloud liquid properties during the two days. On both days a similar vertical profile of liquid properties over pack ice were observed with average droplet concentrations up to 26 cm^{-3} (38 cm^{-3}) on 17 (18) June. In contrast to the warm period the 17 (red) and 18 June (green) LWC profiles follow a linear increase from cloud base to around Z_n =0.5. After this, the liquid water content decreases towards the cloud top due to evaporation induced by entrainment of dry air mass from above cloud. On all days comparison with teoretical adiabatic LWC values (not shown

315 here) show that the observed LWC profiles are subadiabatic. Lowest droplet concentrations, LWC and extinction coefficient were observed for the profile over open sea surface on 18 June (purple). The reduction of LWC in this case can probably be
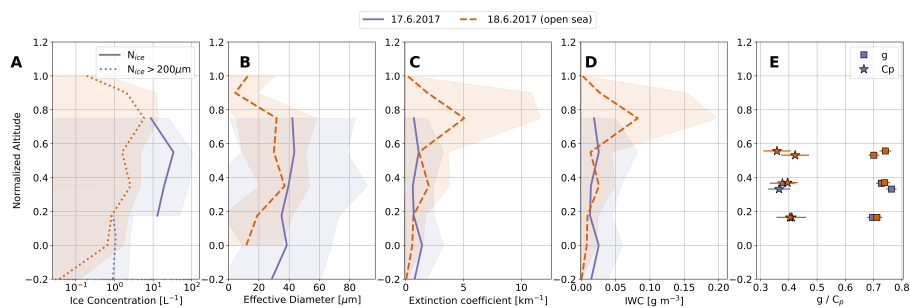
Figure 11. Vertical profile of ice particle concentration (N_{ice}) (A), ice particle effective diameter (B), ice particle extinction coefficient (C) and ice water content (IWC) (D) performed on 17 and 18 June during the normal period. The shaded area illustrates the standard deviations. Note that the ice phase microphysical properties for the vertical profile over open sea surface on 18 June (green) were derived for D >200µm only. Panel E shows the asymmetry parameter (g) and complexity parameter (C_p) derived from PHIPS. One value was derived for each straight leg within the cloud. The horizontal error bars illustrate the retrieval uncertainty.

explained by ongoing glaciation of the cloud through the Wegener-Bergeron-Findeisen process as in the following it is shown that this vertical profile showed the highest IWC. In general droplet concentration, extinction coefficient and LWC were lower than during the warm period but similar to those observed during the cold period.

320   Figure 11 shows the mean vertical profiles of ice phase microphysical properties for 17 June over pack ice and for 18 June over open sea surface. The ice phase microphysical properties on 18 June over pack ice are not shown in Figure 11 since very low ice crystal concentration, below 0.01 L^{-1}, were measured by the CIP, due to relatively warm cloud top temperature of -3°C. On 17 June the mean ice crystal concentrations between 9 and 35 L^{-1} were observed between Z_n of 0.1 and 0.85. The uppermost cloud layer (Z_n >0.85) did not contain ice particles and in the lower parts shattering was observed so that

325   the ice crystal concentrations could be only derived from CIP for D >200µm. The observed extinction coefficient and IWC were around 1 km^{-1} and 0.02 g m^{-3}, similar to what was observed during the warm period. No significant vertical trend was observed in the ice microphysical properties. Since the cloud top temperature was around -5°C it can be argued that rime-splintering was active in the sampled clouds. The dominant ice crystal habits on that day were columns and needles (>85%) with rimed fractions between 20 and 40% (Fig. 12a). Also small unrimed faceted columns and needles were observed, which

330   give indication of an active SIP process in the cloud.

    The highest observed IWC, up to 0.08 g m^{-3}, were observed on 18 June when stratocumulus layer with embedded convective clusters was sampled. Ice crystal concentrations could be only derived for particle with D >200 µm since shattering was observed in the PHIPS and SID-3 probes. Ice crystals with D >200 µm were observed throughout the cloud with an increase in their concentration between Z_n =0.7 and Z_n =0.8 leading to the maximum observed extinction coefficient up to 5 km^{-1}.

335   This was also the only vertical profile that showed a maximum in the extinction coefficient and IWC in the upper half of the cloud. Inspection of the CIP images showed that the increase in ice crystal concentrations between Z_n =0.7 and Z_n =0.8 was caused by predominantly by appearance of columnar type crystal habits, which dominated the upper parts of the cloud. A large

(a) 17 June
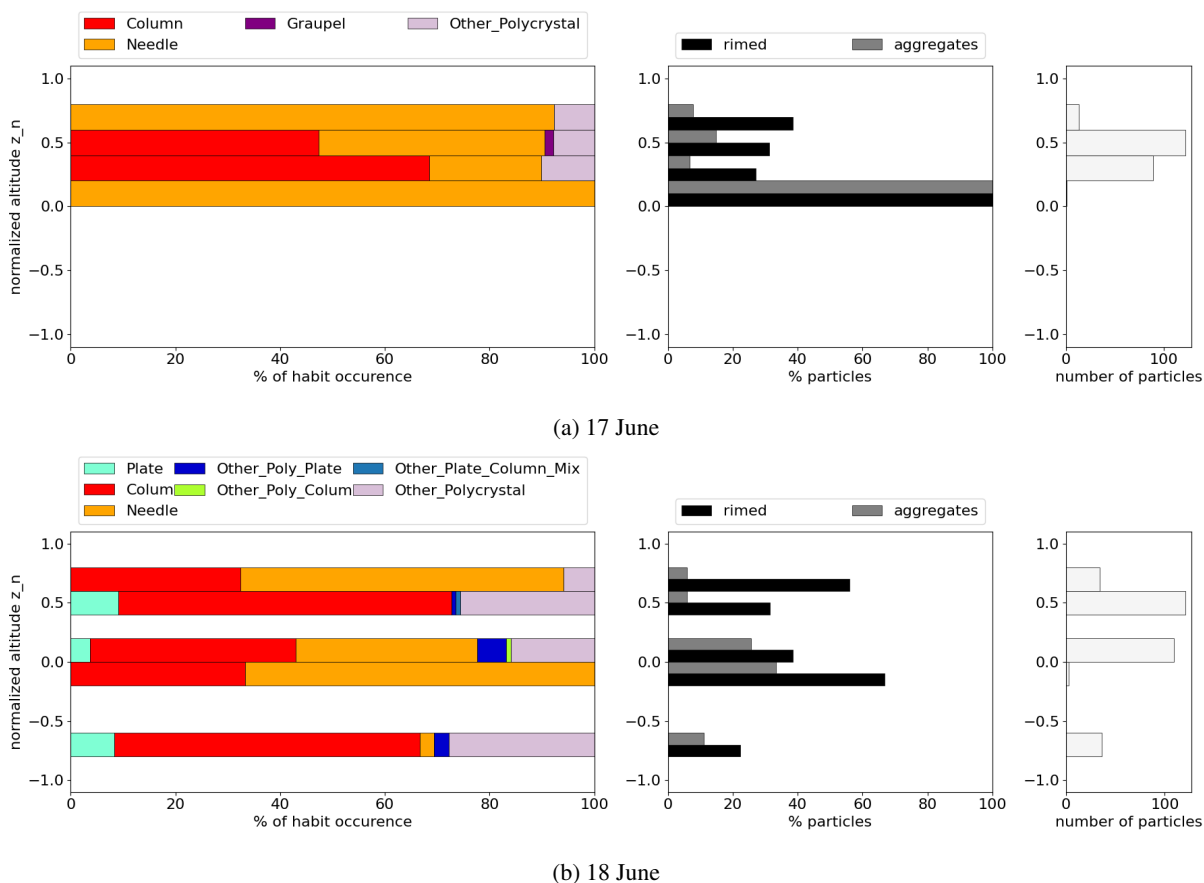
(b) 18 June

Figure 12. Analysis of ice crystal habits during cloud sampling on 17 and 18 June during normal period.

fraction, over 20% of the observed columns were rimed according to the PHIPS images (Fig. 12b). In the lower parts of the cloud both CIP and PHIPS showed also compact polycrystal habits. According to habit statistics based on PHIPS images more

340 polycrystals were observed on the 18 June case compared to other days, between 5.9 and 30.6% (Fig. 12b). Comparable to the warm period profiles, also unrimed small faceted columns and plates were observed during the 18 June profile giving indication of active SIP process.

4 Derived LWP and IWP over pack ice, marginal sea ice zone and open sea surface

In the Arctic, a major cloud feedback is linked with the surface albedo feedback (Curry et al., 1996), which has been estimated

345 to contribute to a significant positive feedback on climate change. Therefore, one objective of the ACLOUD campaign was to investigate the effect of surface albedo (pack ice, marginal sea ice zone or open sea surface) to cloud microphysical properties. Here we discuss a data set of LWPs and IWPs from 15 vertical profiles, from which one was performed over marginal sea ice
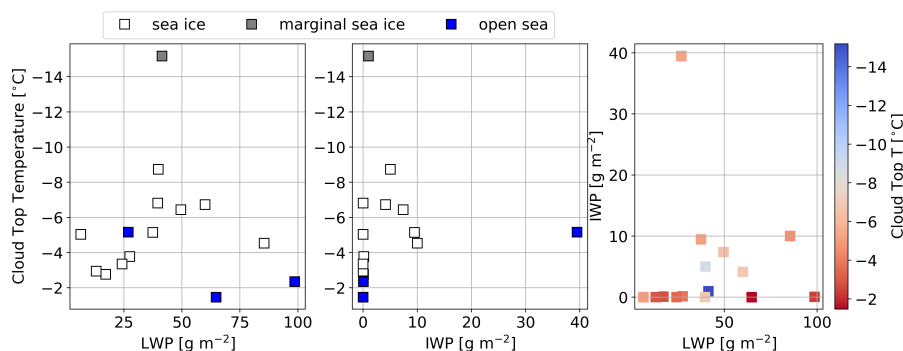
Figure 13. Liquid water path (LWP) and ice water path (IWP) as a function of cloud top temperature during ACLOUD for vertical cloud profiles over pack ice (white symbols), marginal sea ice zone (grey symbols) or open sea surface (blue symbols). The list of vertical cloud profiles can be found in the supplementary material.

zone, 11 over pack ice and 3 over open sea surface. A complete list of these cloud profiles can be found in the supplementary material.

350   The measured cloud LWPs and IWPs varied between 6 and 99 $\mathrm{g\,m^{-2}}$ and 0 and 39 $\mathrm{g\,m^{-2}}$, respectively. The mean LWP and IWP were 42 $\mathrm{gm^{-2}}$ and 5 $\mathrm{g\,m^{-2}}$, respectively. No clear trend with the LWP with cloud top temperature could be seen for the cases presented here. The LWP range observed during ACLOUD is similar to other studies in the European Arctic region where LWPs between 12 and 100 $\mathrm{g\,m^{-2}}$ have been reported (Mioche et al., 2017; Gierens et al., 2020).

For the IWP a clear vertical trend can be seen where up to several orders of magnitude higher IWPs are seen when cloud

355   top temperatures are between -8.7 and - 4.5°C. This increase is likely linked to rime splintering in the Hallett-Mossop (HM) temperature range and subsequent growth of ice splinters in water saturated environment. In two cases the observed IWP in the HM temperature range was below 0.01 $\mathrm{gm^{-2}}$, which can be associated to LWPs below 40 $\mathrm{g\,m^{-2}}$ (Fig. 13). This can indicate that a threshold LWP is needed in stratiform clouds before rime-splintering is triggered. The observed IWP was found to be lower than the Ny Ålesund annual average of 16 $\mathrm{g\,m^{-2}}$ (Gierens et al., 2020) but higher than what was reported by Mioche

360   et al. (2017). For example, in Mioche et al. (2017) no increase in IWP in the Hallett-Mossop temperature range was found.

Since the number of cloud profiles was restricted it is not possible to give statistically meaningful conclusions of the effect of surface to cloud properties. In general higher LWPs are measured over open ocean (mean of 63 $\mathrm{g\,m^{-2}}$) compared to cases over pack ice (mean of 36 $\mathrm{g\,m^{-2}}$), which is also linked to warmer cloud top temperatures for the open sea surface cases.

5   Asymmetry parameter of mixed-phase cloud ice particles

365 For calculating the radiative transfer in clouds at least three cloud particle single-scattering properties are needed: extinction coefficient, single scattering albedo and the asymmetry parameter. From these three single-scattering properties the asymmetry parameter is the most sensitive to the assumed particle microphysical properties in the short-wave. Especially, for aspherical

ice particles the asymmetry parameter is not well constrained. Here we derived the ice crystal asymmetry parameter from partial phase function measured by PHIPS. Since PHIPS detects individual cloud particles, it is possible to derive the cloud
370 asymmetry parameter for ice particles only without the interference of supercooled liquid droplets.

Figures 7E and 11E show the vertical profiles of the ice crystal asymmetry parameters for the cloud cases observed during the warm and normal periods. During the cold period not enough ice crystals were observed by PHIPS in order to investigate the vertical variability of the asymmetry parameter. The observed ice crystal asymmetry parameters varied between 0.69 and 0.76 with the mean ice crystal asymmetry parameter of 0.72. In the lower parts of the cloud no vertical trend in the asymmetry
375 parameter was observed but during the warm period an increase in the asymmetry parameter was seen between $Z_n =$ 0.6 and $Z_n =$ 0.8. This increase in the asymmetry parameter is linked with a simultaneous decrease in the complexity parameter (Fig. 7E). The fraction of less complex particles can be enhanced in the upper parts of the cloud due to generation of faceted crystals by SIP and by higher fall speeds of larger more complex crystals, which would enhance their concentration in the lower parts of the cloud. As the rimed fraction increased with increasing altitude the decrease in crystal complexity cannot be explained
380 by decrease in riming.

The measured ice particle asymmetry parameters found during ACLOUD are significantly lower than those of idealised faceted hexagonal crystals but also lower than previously found in Arctic mixed-phase clouds. Jourdan et al. (2010) performed measurements with the Polar Nephelometer (PN) in an Arctic nimbostratus cloud during the ASTAR campaign in a temperature range between -1 and -12°C. The authors applied principal component analysis to the volume angular scattering measurements
385 to derive asymmetry parameters for ice particles. The lowest asymmetry parameter found using this method was 0.755 that corresponded to a group of columnar crystals mixed with a small fraction of water droplets - similar habits found in our case. Also Mioche et al. (2017) showed measurements of asymmetry parameters associated with Arctic mixed-phase clouds, where asymmetry parameters below 0.8 were observed for the ice phase.

6 Case study of radiative transfer in a single-layer cloud system

390 Our observations have shown that ice is common in spring and summer-time low level Arctic clouds with cloud top temperatures above -10°C. In the same time a low ice crystal asymmetry parameter below 0.75 is observed in the most parts of the clouds. To investigate the role of ice phase for the radiative transfer in an Arctic summer-time low-level clouds with enhanced ice crystal concentrations through rime-splintering we have performed radiative transfer simulations using the one-dimensional plane-parallel discrete ordinate radiative transfer solver (DISORT). Figure 14 displays the vertical distribution of optical thick-
395 ness for ice and water within a cloud. The first three cases are cloud profiles over pack ice during the warm period, while the last case is the convection influenced stratiform case over open sea surface. To evaluate the radiative effects for ice particles, we define the single-wavelength (532 nm) albedo/transmisivity difference as:

$$\Delta R = R_{ice+water} - R_{water}, \tag{8}$$

$$\Delta T = T_{ice+water} - T_{water}, \tag{9}$$

400   where R_{water} and T_{water} are the albedo and transmisivity associated with the cases where ice particles will be treated as liquid water particles, i.e., the ice particles have the same asymmetry parameter as water droplets. On the contrary, $R_{ice+water}$ and $T_{ice+water}$ are associated with the case where ice particles are given their measured asymmetry parameter. The simulation setup is as follows, the surface albedo for the warm period cases are set to be 0.5 to represent the sea ice surface (Stapf et al., 2020), while the surface albedo for the last case is set to be 0.1 to represent the open sea surface (Payne, 1972). The solar zenith

405   angle is set to be 65.9°.

It can be seen that for the warm period cases, the differences for the albedo and transmisivity are generally around or less than 2%, however, for the 18 June case, the albedo and transmisivity differences could be up to ten percent. This highlights the significance of ice scattering effects when ice phase is found at the top of mixed phase clouds. Despite that the 18 June case was a non-typical case during the measurement period, this type of cloud could exert a strong radiative forcing due to the

410   present of ice at the top layer, and highlights the importance of an accurate vertical information of ice extinction within Arctic low-level clouds.

7   Conclusions

As clouds in the Arctic have the potential to insert a positive feedback in a warming climate, it is important to increase the knowledge of the vertical distribution of the cloud water content and phase. Measurements of late spring and summer time

415   stratiform clouds over pack ice, marginal sea ice zone and open water performed during the ACLOUD campaign showed that relatively high ice particle number concentrations up to 35 L^{-1} are observed in cases where cloud top temperatures are between -3.8 and -8.7°C. This elevation in ice crystal number can likely be linked with secondary ice production. Still, the condensed water path is dominated by the liquid phase especially at the cloud top in most of the studied cases except in one case study of a system with embedded convection where ice extinction exceeded the liquid extinction. Simultaneous measurements of

420   ice optical properties showed that a relative low asymmetry parameters between 0.69 and 0.76 can be associated with the mixed-phase cloud ice crystals.

The presented results highlight that there exists a non-linear relationship between cloud top temperature and ice crystal concentration. It is well known that the ice phase has an important role for the cloud lifetime but here we showed, that the ice phase in low-level mixed-phase clouds, otherwise dominated by liquid phase, can also be radiatively important in cases where

425   ice phase contributes to the cloud top extinction. In such cases the ice single-scattering properties, such as the asymmetry parameter, need to be well known. In order to accurately predict Arctic warming, it is important that models capture the cloud microphysical processes in Arctic clouds. In-situ observations provide an important basis for testing and improving microphysical parameterisations.
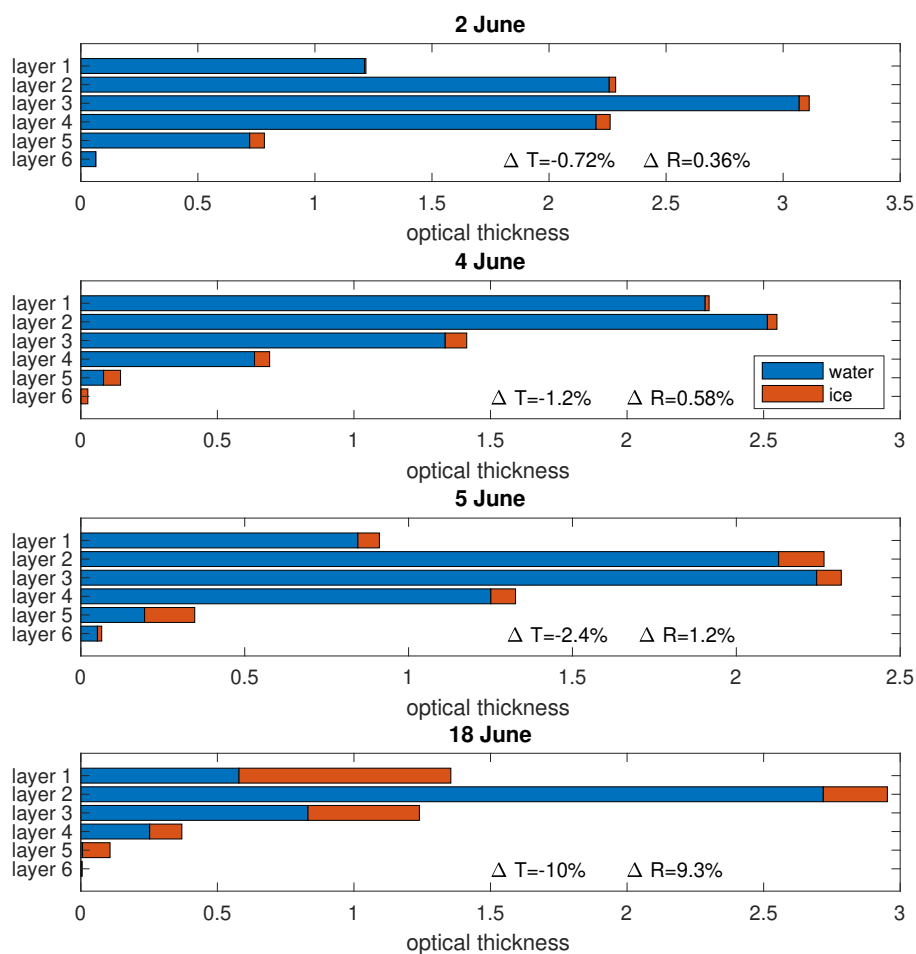
Figure 14. The optical thickness for water and ice for different altitudes within the cloud. Cases are as the following: case 1 represents the 2 June cloud case, case 2 the 4 June cloud case, case 3 the 5 June cloud case and case 4 the 18 June cloud case.

Data availability. The observational data from the ACLOUD campaign are archived on the PANGAEA repository and can be accessed from
430 the DOIs given in the references.

Appendix A: Machine learning algorithm to detect co-incidence artefacts in SID-3 scattering patterns

The SID-3 camera has a theoretical coincidence sampling probability of 1% for a particle number concentration of 103 cm^{-3} (Vochezer et al., 2016). Coincidence sampling typically occurs for two droplets so that instead of a scattering pattern with

concentric rings (see Fig. A1a) a distorted scattering pattern, e.g., a "kidney" shaped shadow, is recorded (see Figs. A1c or

435 A1d). Coincidence patterns are always classified as aspherical particles by the automatic classification scheme, so that in a mixed-phase cloud environment a coincidence sampling probability of 1% would lead to a significant overestimation of ice concentration. However, due to the high-resolution of the SID-3 2-D scattering patterns the coincidence affected patterns are easily identifiable by human eye. Since manual re-classification of coincidence patterns is very time-demanding as SID-3 typically acquires in the order of ∼100.000 images per flight, here, we have trained a deep learning neural net that classifies

440 particles measured by SID-3 based on their 2-D scattering pattern.
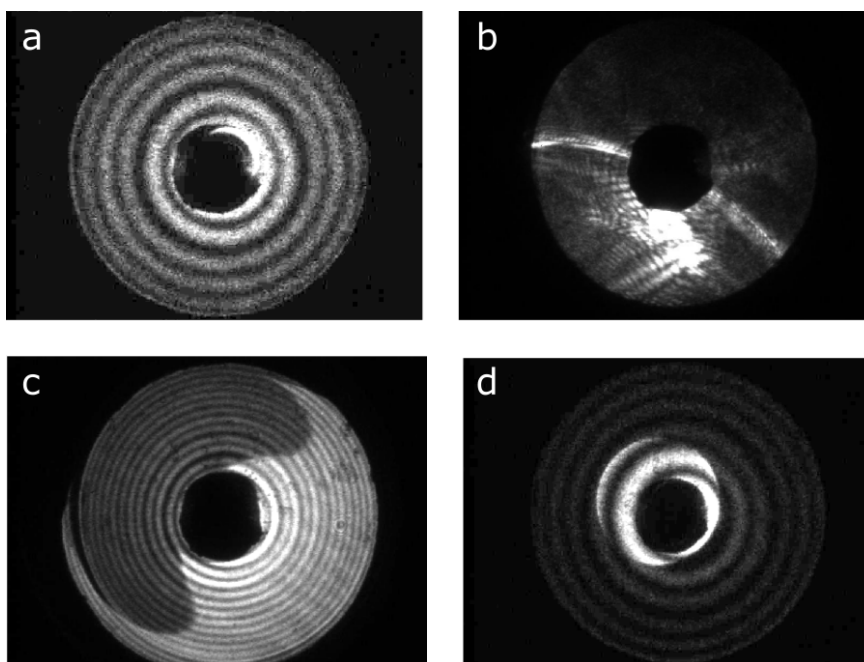
Figure A1. Measured SID-3 scattering patterns of exemplary particles: droplet (a), ice particle (b), coinciding droplets (c,d).

A1 Data Basis

The data used to train and validate the net consists of a subset of i) previously manually classified particles from the ACLOUD campaign and ii) particles from cloud segments where SID-3 flew in pure ice or pure liquid cloud clouds during the CIRRUS-HL and ACLOUD campaigns.

445 Set i), the manually classified data, consists of 460.000 droplets, 75.000 coincidence events and 2488 ice particles. Only images with mean-intensity between 10 and 50 were manually classified (about 50% of all ACLOUD data) to remove coincidence artefacts from crystal complexity analysis performed in Järvinen et al. (2018). As this set is heavily biased towards liquid, the following subset of 4.000 particles was selected at random out of each category: 1.000 particles that were both classified as liquid by the discrimination algorithm and the manual classification (true liquid) and 1.000 particles that were classified as

450 ice by the algorithm but identified as coincidence events by manual classification (false ice) and 2.000 ice particles that were identified by both the algorithm and manual classification (true ice).

Set ii) consists of cases where SID-3 flew in a pure ice cloud (CIRRUS-HL flight RF12) and a pure liquid cloud (ACLOUD flight on 17.6.2017). To match the numbers of subset i), 2.000 particles were selected at random from each flight. During the ACLOUD liquid case, an estimated 14% of all images were coincidence droplets. Note that these data are not restricted based

455 on the image mean-intensity range as the manually classified particles in i).

Combined, subsets i) and ii) consist of a total of 8.000 particles, equal parts liquid and ice, which are split in half as training and validation data sets. Both data sets consist of in total 4.000 particles each, 1.000 manually classified ice particles, 1.000 ice particles recorded in a cirrus cloud, manually classified 500 true droplets and 500 coincidence droplets, 1.000 droplets recorded in a warm (T>0°C) cloud. These particles are chosen at random out of the above mentioned data set. The training and

460 validation data set are completely disjunctive, i.e. the net is validated on data it has not yet seen before during training.

The single particle 2-D scattering pattern is saved as a 780x582 px 8-bit image as a .jpg file. Due to limited GPU RAM and to reduce computation time of the neural net, each image was scaled down by x1/10 from 780x582 px to 78x89 px.

A2 Neural Net

Based on this data, a deep learning neural net was trained. It was set up using the embedded deep learning environment in

465 MATLAB (MATrix LABoratory) consisting of a 2-D [59x78] image input layer, a 2-D convolutional layer with 64 filters of size [5 5], a batch normalization layer, a rectified linear unit (ReLU) layer, a 2-D max pooling layer with pool size [2 2] and stride [2 2], two fully connected layers with output sizes 10 and 2, a softmax layer and finally the binary classification layer (1/0, corresponding to liquid/ice). The solver is a stochastic gradient descent with momentum (SGDM) optimizer with initial learning rate of 0.05 and a maximum number of epochs of 15.

470 A3 Discrimination Accuracy

Fig. A2 shows the confusion matrix for the validation data set. The net classifies 98.8% of all droplets correctly (i.e., in a liquid cloud 1.1% of particles are classified as ice). For ice particles, the accuracy is 99.1%. This a better accuracy compared to the original algorithm which had a misclassification rate of 2%-20%, depending on particle density and hence coincidence rate. Interestingly, the true coincidence rate observed in the training data set was significantly higher than the theoretical expected

475 coincidence rate of 1% for the expected droplet concentrations. This indicates that droplets might be located in concentrated pockets within the cloud increasing the coincidence probability, or, that shattering of larger ice particles might cause shattering fragments to coincide in the camera field-of-view.

A misclassification rate of 1.1% can still result in a significant overestimation of ice by a factor of 2 to 10. Therefore, we combined the neural net analysis with manual inspection in the following way: if a particle was classified as spherical

480 (liquid) by either the original algorithm or the neural net, it was considered liquid. During ACLOUD the remaining number of 2-D scattering patterns where both or either the original algorithm or the neural net classified a particle as aspherical (ice) was typically low enough (around 100 - 1.000 per flight) so that those 2-D scattering patterns were manually inspected and
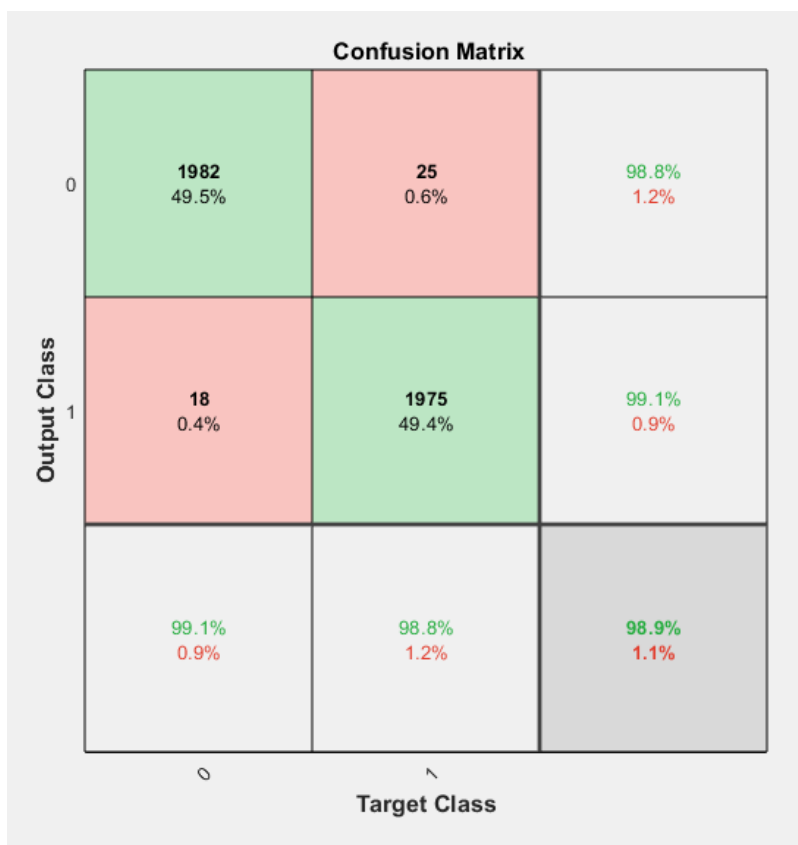
Figure A2. Confusion matrix that visualizes the classification accuracy of the phase discrimination neural net based on the validation data set.

reclassified if necessary. The SID-3 ice concentration shown in this paper can, therefore, be considered as the lower limit for ice concentrations below 50 μm.

485 *Author contributions.* MS and EJ operated the SID-3 and PHIPS instruments during the ACLOUD campaign. OJ, RD and GM operated the CIP instrument during ACLOUD. EJ, FN, FW and MS analysed the SID-3 and PHIPS data and OJ, RD and GM analysed the CIP data. GZ performed the radiative transfer calculations. All were contributing to the interpretation of the results. EJ wrote the manuscript with help of all co-authors.

Competing interests. Martin Schnaiter and Emma Järvinen are members of schnaiTEC GmbH that manufactures a commercial version of
490 the PHIPS instrument. Martin Schnaiter is part-time employed by schnaiTEC GmbH.

Acknowledgements. This work received funding through the Helmholtz Association's Initiative and Networking Fund (grant agreement no. VH-NG-1531), the Helmholtz Association research program "Atmosphere and Climate". MS acknowledges funding from the German Research Foundation (grants SCHN 1140/3-1 and SCHN 1140/3-2). FW acknowledges funding by the German Research Foundation (DFG grant JA 2818/1-1). The LaMP acknowledges the support of the (MPC2-EAn n°1224) project funded by the Institut Polaire Paul Emile Victor (IPEV) and the Pollution in the Arctic System (PARCS) project funded by the Chantier Arctique of the Centre National de la Recherche Scientifique-Institut National des Sciences de l'Univers (CNRS-INSU).

References

Abdelmonem, A., Järvinen, E., Duft, D., Hirst, E., Vogt, S., Leisner, T., and Schnaiter, M.: PHIPS–HALO: the airborne Particle Habit Imaging and Polar Scattering probe – Part 1: Design and operation, Atmos. Meas. Tech., 9, 3131–3144, 2016.

500 Bailey, M. P. and Hallett, J.: A Comprehensive Habit Diagram for Atmospheric Ice Crystals: Confirmation from the Laboratory, AIRS II, and Other Field Studies, Journal of the Atmospheric Sciences, 66, 2888 – 2899, https://doi.org/10.1175/2009JAS2883.1, 2009.

Baumgardner, D., Jonsson, H., Dawson, W., O'Connor, D., and Newton, R.: The cloud, aerosol and precipitation spectrometer: a new instrument for cloud investigations, Atmospheric Research, 59-60, 251–264, https://doi.org/https://doi.org/10.1016/S0169-8095(01)00119-3, 13th International Conference on Clouds and Precipitation, 2001.

505 Baumgardner, D., Abel, S. J., Axisa, D., Cotton, R., Crosier, J., Field, P., Gurganus, C., Heymsfield, A., Korolev, A., Krämer, M., Lawson, P., McFarquhar, G., Ulanowski, Z., and Um, J.: Cloud Ice Properties: In Situ Measurement Challenges, Meteorological Monographs, 58, 9.1–9.23, https://doi.org/10.1175/amsmonographs-d-16-0011.1, 2017.

Brown, P. R. A. and Francis, P. N.: Improved Measurements of the Ice Water Content in Cirrus Using a Total-Water Probe, Journal of Atmospheric and Oceanic Technology, 12, 410 – 414, https://doi.org/10.1175/1520-0426(1995)012<0410:IMOTIW>2.0.CO;2, 1995.

510 Cai, Y., Montague, D. C., Mooiweer-Bryan, W., and Deshler, T.: Performance characteristics of the ultra high sensitivity aerosol spectrometer for particles between 55 and 800nm: Laboratory and field studies, Journal of Aerosol Science, 39, 759–769, https://doi.org/https://doi.org/10.1016/j.jaerosci.2008.04.007, 2008.

Crosier, J., Bower, K. N., Choularton, T. W., Westbrook, C. D., Connolly, P. J., Cui, Z. Q., Crawford, I. P., Capes, G. L., Coe, H., Dorsey, J. R., Williams, P. I., Illingworth, A. J., Gallagher, M. W., and Blyth, A. M.: Observations of ice multiplication in a weakly convective cell

515 embedded in supercooled mid-level stratus, Atmospheric Chemistry and Physics, 11, 257–273, https://doi.org/10.5194/acp-11-257-2011, 2011.

Curry, J. A. and Ebert, E. E.: Annual cycle of radiation fluxes over the Arctic Ocean: Sensitivity to cloud optical properties, Journal of Climate, 5, 1267–1280, 1992.

Curry, J. A., Schramm, J. L., Rossow, W. B., and Randall, D.: Overview of Arctic cloud and radiation characteristics, Journal of Climate, 9,

520 1731–1764, 1996.

Dupuy, R., Jourdan, O., Mioche, G., Ehrlich, A., Waitz, F., Gourbeyre, C., Järvinen, E., Schnaiter, M., and Schwarzenböck, A.: CLOUD MICROPHYSICAL PROPERTIES OF SUMMERTIME ARCTIC STRATOCUMULUS DURING THE ACLOUD CAM- PAIGN : COMPARISON WITH PREVIOUS RESULTS IN THE EUROPEAN ARCTIC., https://doi.org/10.1594/PANGAEA.899074, Vancouver, Canada. hal-01932907, 2018.

525 Dupuy, R., Jourdan, O., Mioche, G., Gourbeyre, C., Leroy, D., and Schwarzenböck, A.: CDP, CIP and PIP In-situ arctic cloud microphysical properties observed during ACLOUD-AC3 campaign in June 2017, LAMP/CNRS/UCA/OPGC, PANGAEA, https://doi.org/10.1594/PANGAEA.899074, 2019.

Field, P., Heymsfield, A., and Bansemer, A.: Shattering and particle interarrival times measured by optical array probes in ice clouds, Journal of Atmospheric and Oceanic Technology, 23, 1357–1371, 2006.

530 Fridlind, A. M., Ackerman, A., McFarquhar, G., Zhang, G., Poellot, M., DeMott, P., Prenni, A., and Heymsfield, A.: Ice properties of single-layer stratocumulus during the Mixed-Phase Arctic Cloud Experiment: 2. Model results, Journal of Geophysical Research: Atmospheres, 112, 2007.

Gierens, R., Kneifel, S., D. Shupe, M., Ebell, K., Maturilli, M., and Löhnert, U.: Low-level mixed-phase clouds in a complex Arctic environment, Atmospheric Chemistry and Physics, 20, 3459–3481, https://doi.org/10.5194/acp-20-3459-2020, 2020.

535 Hartmann, J., Gehrmann, M., Kohnert, K., Metzger, S., and Sachs, T.: New calibration procedures for airborne turbulence measurements and accuracy of the methane fluxes during the AirMeth campaigns, Atmospheric Measurement Techniques, 11, 4567–4581, https://doi.org/10.5194/amt-11-4567-2018, 2018.

Hartmann, J., L. C. and Chechin, D.: 1Hz resolution aircraft measurements of wind and temperature during the ACLOUD campaign in 2017, Alfred Wegener Institute, Helmholtz Centre for Polar and Marine Research, Bremerhaven, PANGAEA,
540 https://doi.org/10.1594/PANGAEA.902849, 2019.

Hirst, E., Kaye, P., Greenaway, R., Field, P., and Johnson, D.: Discrimination of micrometre-sized ice and super-cooled droplets in mixed-phase cloud, Atmospheric Environment, 35, 33–47, https://doi.org/https://doi.org/10.1016/S1352-2310(00)00377-0, 2001.

Jackson, R. C., McFarquhar, G. M., Korolev, A. V., Earle, M. E., Liu, P. S. K., Lawson, R. P., Brooks, S., Wolde, M., Laskin, A., and Freer, M.: The dependence of ice microphysics on aerosol concentration in arctic mixed-phase stratus clouds during ISDAC and M-PACE, Journal
545 of Geophysical Research: Atmospheres, 117, https://doi.org/https://doi.org/10.1029/2012JD017668, 2012.

Järvinen, E., Jourdan, O., Neubauer, D., Yao, B., Liu, C., Andreae, M. O., Lohmann, U., Wendisch, M., McFarquhar, G. M., Leisner, T., and Schnaiter, M.: Additional global climate cooling by clouds due to ice crystal complexity, Atmospheric Chemistry and Physics, 18, 15 767–15 781, https://doi.org/10.5194/acp-18-15767-2018, 2018.

Jourdan, O., Mioche, G., Garrett, T. J., Schwarzenböck, A., Vidot, J., Xie, Y., Shcherbakov, V., Yang, P., and Gayet, J. F.: Coupling of the
550 microphysical and optical properties of an Arctic nimbostratus cloud during the ASTAR 2004 experiment: Implications for light-scattering modeling, Journal of Geophysical Research Atmospheres, 115, 1–16, https://doi.org/10.1029/2010JD014016, 2010.

Järvinen, E., McCluskey, C. S., Waitz, F., Schnaiter, M., Bansemer, A., Bardeen, C. G., Gettelman, A., Heymsfield, A., Stith, J. L., Wu, W., D'Alessandro, J. J., McFarquhar, G. M., Diao, M., Finlon, J. A., Hill, T. C. J., Levin, E. J. T., Moore, K. A., and DeMott, P. J.: Evidence for Secondary Ice Production in Southern Ocean Maritime Boundary Layer Clouds, Journal of Geophysical Research: Atmospheres, 127,
555 e2021JD036 411, https://doi.org/https://doi.org/10.1029/2021JD036411, e2021JD036411 2021JD036411, 2022.

Kahl, J. D.: Characteristics of the low-level temperature inversion along the Alaskan Arctic coast, International Journal of Climatology, 10, 537–548, 1990.

Kahl, J. D., Serreze, M. C., and Schnell, R. C.: Tropospheric low-level temperature inversions in the Canadian Arctic, Atmosphere-Ocean, 30, 511–529, 1992.

560 Kanji, Z. A., Ladino, L. A., Wex, H., Boose, Y., Burkert-Kohn, M., Cziczo, D. J., and Krämer, M.: Overview of Ice Nucleating Particles, Meteorological Monographs, 58, 1.1 – 1.33, https://doi.org/10.1175/AMSMONOGRAPHS-D-16-0006.1, 2017.

Knudsen, E. M., Heinold, B., Dahlke, S., Bozem, H., Crewell, S., Gorodetskaya, I. V., Heygster, G., Kunkel, D., Maturilli, M., Mech, M., Viceto, C., Rinke, A., Schmithüsen, H., Ehrlich, A., Macke, A., Lüpkes, C., and Wendisch, M.: Meteorological conditions during the ACLOUD/PASCAL field campaign near Svalbard in early summer 2017, Atmospheric Chemistry and Physics, 18, 17 995–18 022,
565 https://doi.org/10.5194/acp-18-17995-2018, 2018.

Korolev, A. V., Isaac, G. A., and Hallett, J.: Ice particle habits in Arctic clouds, Geophysical Research Letters, 26, 1299–1302, https://doi.org/10.1029/1999GL900232, 1999.

Lawson, R. P., Baker, B. A., Schmitt, C. G., and Jensen, T. L.: An overview of microphysical properties of Arctic clouds observed in May and July 1998 during FIRE ACE, Journal of Geophysical Research: Atmospheres, 106, 14 989–15 014,
570 https://doi.org/https://doi.org/10.1029/2000JD900789, 2001.

Lloyd, G., Choularton, T. W., Bower, K. N., Crosier, J., Jones, H., Dorsey, J. R., Gallagher, M. W., Connolly, P., Kirchgaessner, A. C., and Lachlan-Cope, T.: Observations and comparisons of cloud microphysical properties in spring and summertime Arctic stratocumulus clouds during the ACCACIA campaign, Atmospheric Chemistry and Physics, 15, 3719–3737, https://doi.org/10.5194/acp-15-3719-2015, 2015.

575 McFarquhar, G. M., Zhang, G., Poellot, M. R., Kok, G. L., McCoy, R., Tooman, T., Fridlind, A., and Heymsfield, A. J.: Ice properties of single-layer stratocumulus during the Mixed-Phase Arctic Cloud Experiment: 1. Observations, Journal of Geophysical Research Atmospheres, 112, 1–19, https://doi.org/10.1029/2007JD008633, 2007.

Mertes, S.; Kästner, U. M. A.: Airborne in-situ measurements of the aerosol absorption coefficient, aerosol particle number concentration and size distribution of cloud particle residuals and ambient aerosol particles during the ACLOUD campaign in May and June 2017.
580 Leibniz-Institut für Troposphärenforschung e.V., Leipzig, PANGAEA, https://doi.org/10.1594/PANGAEA.900403, 2019.

Mioche, G., Jourdan, O., Ceccaldi, M., and Delanoë, J.: Variability of mixed-phase clouds in the Arctic with a focus on the Svalbard region: a study based on spaceborne active remote sensing, Atmospheric Chemistry and Physics, 15, 2445–2461, https://doi.org/10.5194/acp-15-2445-2015, 2015.

Mioche, G., Jourdan, O., Delanoë, J., Gourbeyre, C., Febvre, G., Dupuy, R., Monier, M., Szczap, F., Schwarzenboeck, A., and Gayet, J. F.:
585 Vertical distribution of microphysical properties of Arctic springtime low-level mixed-phase clouds over the Greenland and Norwegian seas, Atmospheric Chemistry and Physics, 17, 12 845–12 869, https://doi.org/10.5194/acp-17-12845-2017, 2017.

Morrison, H., de Boer, G., Feingold, G., Harrington, J., Shupe, M. D., and Sulia, K.: Resilience of persistent Arctic mixed-phase clouds, Nature Geoscience, 5, 11–17, https://doi.org/10.1038/ngeo1332, 2012.

Mossop, S.: Microphysical properties of supercooled cumulus clouds in which an ice particle multiplication process operated, Quarterly
590 Journal of the Royal Meteorological Society, 111, 183–198, 1985.

Pasquier, J. T., Henneberger, J., Ramelli, F., Lauber, A., David, R. O., Wieder, J., Carlsen, T., Gierens, R., Maturilli, M., and Lohmann, U.: Conditions favorable for secondary ice production in Arctic mixed-phase clouds, Atmospheric Chemistry and Physics Discussions, pp. 1–33, 2022.

Payne, R. E.: Albedo of the sea surface, Journal of Atmospheric Sciences, 29, 959–970, 1972.

595 Previdi, M., Smith, K. L., and Polvani, L. M.: Arctic amplification of climate change: a review of underlying mechanisms, Environmental Research Letters, 16, 093 003, 2021.

Rangno, A. L. and Hobbs, P. V.: Ice particles in stratiform clouds in the Arctic and possible mechanisms for the production of high ice concentrations, Journal of Geophysical Research Atmospheres, 106, 15 065–15 075, https://doi.org/10.1029/2000JD900286, 2001.

Rigor, I. G., Colony, R. L., and Martin, S.: Variations in surface air temperature observations in the Arctic, 1979–97, Journal of Climate, 13,
600 896–914, 2000.

Schnaiter, M. and Järvinen, E.: SID-3 1Hz size distribu- tion of cloud particles during the ACLOUD campaign in 2017, Karlsruher Institut für Technologie, Institut für Meteorologie und Klimaforschung, Karlsruhe, PANGAEA, https://doi.org/10.1594/PANGAEA.900261, 2019a.

Schnaiter, M. and Järvinen, E.: SID-3 analysis results for 2D scattering patterns during the ACLOUD campaign in 2017, Karlsruher Institut für Technologie, Institut für Me- teorologie und Klimaforschung, Karlsruhe, PANGAEA, https://doi.org/10.1594/PANGAEA.900380,
605 2019b.

Schnaiter, M. and Järvinen, E.: PHIPS particle-by-particle data for the ACLOUD campaign in 2017, Karlsruher Institut für Technologie, Institut für Me- teorologie und Klimaforschung, Karlsruhe, PANGAEA, https://doi.org/10.1594/PANGAEA.902611, 2019c.

Schnaiter, M., Järvinen, E., Vochezer, P., Abdelmonem, A., Wagner, R., Jourdan, O., Mioche, G., Shcherbakov, V. N., Schmitt, C. G., Tricoli, U., Ulanowski, Z., and Heymsfield, A. J.: Cloud chamber experiments on the origin of ice crystal complexity in cirrus clouds, Atmospheric Chemistry and Physics, 16, 5091–5110, https://doi.org/10.5194/acp-16-5091-2016, 2016.

Schnaiter, M., Järvinen, E., Abdelmonem, A., and Leisner, T.: PHIPS-HALO: the airborne particle habit imaging and polar scattering probe – Part 2: Characterization and first results, Atmos. Meas. Tech., 11, 341–357, 2018.

Serreze, M., Barrett, A., Stroeve, J., Kindig, D., and Holland, M.: The emergence of surface-based Arctic amplification, The Cryosphere, 3, 11–19, 2009.

Serreze, M. C., Kahl, J. D., and Schnell, R. C.: Low-level temperature inversions of the Eurasian Arctic and comparisons with Soviet drifting station data, Journal of Climate, 5, 615–629, 1992.

Shupe, M. D. and Intrieri, J. M.: Cloud Radiative Forcing of the Arctic Surface: The Influence of Cloud Properties, Surface Albedo, and Solar Zenith Angle, Journal of Climate, 17, 616 – 628, https://doi.org/10.1175/1520-0442(2004)017<0616:CRFOTA>2.0.CO;2, 2004.

Sotiropoulou, G., Sullivan, S., Savre, J., Lloyd, G., Lachlan-Cope, T., Ekman, A. M. L., and Nenes, A.: The impact of secondary ice production on Arctic stratocumulus, Atmospheric Chemistry and Physics, 20, 1301–1316, https://doi.org/10.5194/acp-20-1301-2020, 2020.

Spreen, G., Kaleschke, L., and Heygster, G.: Sea ice remote sensing using AMSR-E 89-GHz channels, Journal of Geophysical Research: Oceans, 113, https://doi.org/https://doi.org/10.1029/2005JC003384, 2008.

Stapf, J., Ehrlich, A., Jäkel, E., Lüpkes, C., and Wendisch, M.: Reassessment of shortwave surface cloud radiative forcing in the Arctic: consideration of surface-albedo–cloud interactions, Atmospheric Chemistry and Physics, 20, 9895–9914, 2020.

Vochezer, P., Jarvinen, E., Wagner, R., Kupiszewski, P., Leisner, T., and Schnaiter, M.: In situ characterization of mixed phase clouds using the Small Ice Detector and the Particle Phase Discriminator, Atmospheric Measurement Techniques, 9, https://doi.org/10.5194/amt-9-159-2016, 2016.

Waitz, F., Schnaiter, M., Leisner, T., and Järvinen, E.: PHIPS–HALO: the airborne Particle Habit Imaging and Polar Scattering probe – Part 3: Single-particle phase discrimination and particle size distribution based on the angular-scattering function, Atmospheric Measurement Techniques, 14, 3049–3070, https://doi.org/10.5194/amt-14-3049-2021, 2021.

Wendisch, M., MacKe, A., Ehrlich, A., LüPkes, C., Mech, M., Chechin, D., Dethloff, K., Velasco, C. B., Bozem, H., BrüCkner, M., Clemen, H. C., Crewell, S., Donth, T., Dupuy, R., Ebell, K., Egerer, U., Engelmann, R., Engler, C., Eppers, O., Gehrmann, M., Gong, X., Gottschalk, M., Gourbeyre, C., Griesche, H., Hartmann, J., Hartmann, M., Heinold, B., Herber, A., Herrmann, H., Heygster, G., Hoor, P., Jafariserajehlou, S., JäKel, E., JäRvinen, E., Jourdan, O., KäStner, U., Kecorius, S., Knudsen, E. M., KöLlner, F., Kretzschmar, J., Lelli, L., Leroy, D., Maturilli, M., Mei, L., Mertes, S., Mioche, G., Neuber, R., Nicolaus, M., Nomokonova, T., Notholt, J., Palm, M., Van Pinxteren, M., Quaas, J., Richter, P., Ruiz-Donoso, E., SchäFer, M., Schmieder, K., Schnaiter, M., Schneider, J., SchwarzenböCk, A., Seifert, P., Shupe, M. D., Siebert, H., Spreen, G., Stapf, J., Stratmann, F., Vogl, T., Welti, A., Wex, H., Wiedensohler, A., Zanatta, M., Zeppenfeld, and Sebastian: The arctic cloud puzzle using acloud/pascal multiplatform observations to unravel the role of clouds and aerosol particles in arctic amplification, Bulletin of the American Meteorological Society, 100, 841–871, https://doi.org/10.1175/BAMS-D-18-0072.1, 2019.

Xu, G., Schnaiter, M., and Järvinen, E.: Accurate Retrieval of Asymmetry Parameter for Large and Complex Ice Crystals From In-Situ Polar Nephelometer Measurements, Journal of Geophysical Research: Atmospheres, 127, 1–19, https://doi.org/10.1029/2021jd036071, 2022.

Zhao, X., Liu, X., Phillips, V. T. J., and Patade, S.: Impacts of secondary ice production on Arctic mixed-phase clouds based on ARM observations and CAM6 single-column model simulations, Atmospheric Chemistry and Physics, 21, 5685–5703, https://doi.org/10.5194/acp-21-5685-2021, 2021.